

Absolute/Convective Instabilities and Front Propagation in Lipid Membrane Tubes

Joël Tchoufag,^{1, *} Amaresh Sahu,^{1, ‡} and Kranthi K. Mandadapu^{1,2, †}

¹Department of Chemical & Biomolecular Engineering, University of California, Berkeley, CA 94720

²Chemical Sciences Division, Lawrence Berkeley National Laboratory, Berkeley, CA 94720

(Dated: April 5, 2022)

We analyze the stability of biological membrane tubes, with and without a base flow of lipids. Membrane dynamics are completely specified by two dimensionless numbers: the well-known Föppl–von Kármán number Γ and the recently introduced Scriven–Love number SL , respectively quantifying the base tension and base flow speed. For unstable tubes, the growth rate of a local perturbation depends only on Γ , whereas SL governs the absolute or convective nature of the instability. Furthermore, nonlinear simulations of unstable tubes reveal an initially localized disturbance results in propagating fronts, which leave a thin atrophied tube in their wake. Depending on the value of Γ , the thin tube is connected to the unperturbed regions via oscillatory or monotonic shape transitions—reminiscent of recent experimental observations on the retraction and atrophy of axons. We elucidate our findings through a weakly nonlinear analysis, which shows membrane dynamics may be approximated by a model of the class of extended Fisher–Kolmogorov equations. This model possesses Lifshitz points, where the front dynamics undergo a steady-to-oscillatory bifurcation, thus shedding light on the pattern selection mechanism in neurons.

Keywords: lipid membrane tube; absolute/convective instability; front propagation

Lipid membranes are ubiquitous in biology, as they constitute the cell boundary and the boundary of the cell’s internal organelles. In both *in vivo* and *in vitro* systems, lipid membranes are often found in cylindrical shapes [1–4]. When membrane tubes are under high tension, they can undergo shape instabilities leading to new morphologies. Such dynamical shape changes are triggered through various disturbances, which can be classified as either *global* or *local* perturbations. In the former case, tubes are disturbed along their entire length, for example via spontaneous thermal fluctuations [5], an applied extensional flow [6, 7] or osmotic shocks [8–10]—with pearled configurations always ensuing. When a tube is perturbed locally, on the other hand, different morphologies result from the initial disturbance invading the unstable tube via propagating fronts. For example, when a laser is aimed at a point on a membrane tether, pearls form in the wake of the moving fronts [5, 11–13]. In contrast, focused laser beam ablation applied to *in vitro* cultures of axons results in a thin atrophied tube, which is connected to the unperturbed region via either a modulated or monotonic transition [14]—the latter being similar to the nonlinear simulation results reported in Fig. 1(b). Additionally, drug treatments disrupting actin filaments and microtubules in axons revealed that fronts only propagate from the neuron’s growth cone to its cell body [14]. However, the physical mechanisms governing these behaviors, namely (i) the pattern selection in the membrane region connecting thin atrophied tubes to moving fronts and (ii) the direction of instability propagation, remain poorly understood.

In this Letter, we shed light on the aforementioned mechanisms by incorporating two often overlooked traits into our description of membrane tubes. First, while most studies of cylindrical membrane instabilities assume

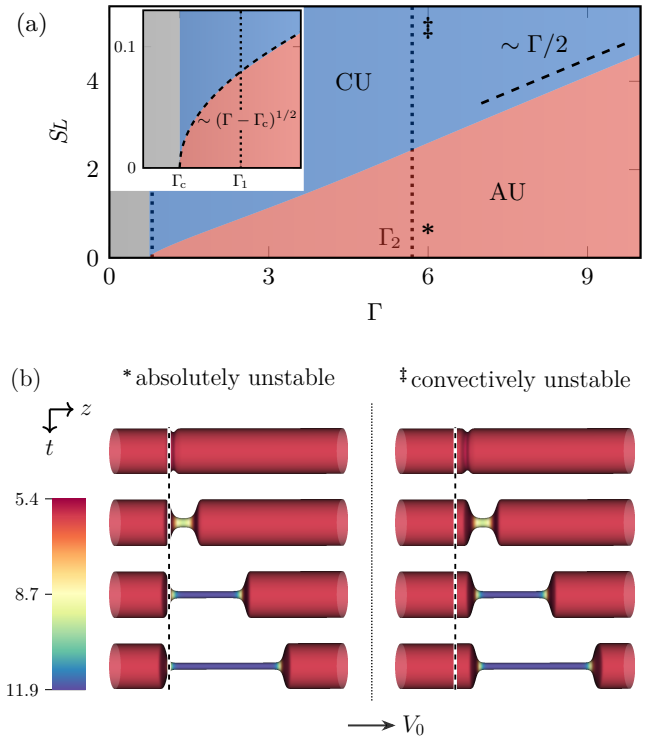


FIG. 1. (a) Stability diagram of lipid membrane tubes in the space of Γ and SL , showing stable (gray, $\Gamma < \Gamma_c = 3/4$), absolutely unstable (AU, red), and convectively unstable (CU, blue) regimes. The critical velocity of the AU/CU transition scales as $\Gamma/2$ at large Γ , but as $(\Gamma - \Gamma_c)^{1/2}$ for $\Gamma \rightarrow \Gamma_c^+$ (see inset). Dashed vertical lines mark the interval (Γ_1, Γ_2) where fronts invading the undeformed tube are oscillatory. At the points marked ‘*’ and ‘‡’, snapshots from nonlinear simulations (b) reveal propagating fronts. The initial perturbation is at the vertical dashed line, flow is in the positive z -direction, the color bar indicates the surface tension, and for clarity the snapshots are scaled by a factor of 40 in the z -direction.

the bulk fluid viscosity is the main source of dissipation [5, 13, 15–20], here we consider the intramembrane viscosity to be the primary dissipative cause. Second, due to the flow of lipids observed in both axons (where speeds reach up to $\sim 10 \mu\text{m}/\text{min}$) [21, 22] and membrane tethers bridging spherical vesicles [23], we incorporate a base flow of lipids in our description. In what follows, we begin by presenting the dimensionless equation governing cylindrical membrane dynamics, from which we obtain the dispersion relation. We then elucidate the effects of a nonzero base flow of lipids on membrane spatiotemporal stability. In particular, we demonstrate the relevance of the hydrodynamic concepts of *absolute* and *convective* instabilities [24, 25] to understanding the long-time behavior of lipid membrane tubes subjected to initially localized perturbations. We next investigate the dynamics of how the fronts ensuing from a local perturbation invade the unperturbed membrane tube. We employ the so-called marginal stability criterion (MSC) [26, 27], and corroborate our analytical results with direct simulations and a weakly nonlinear analysis of the shape evolution of an unstable tube. Importantly, we find both atrophied and pearled morphologies can result from a local perturbation, and our front speed calculations qualitatively agree with previous experimental measurements.

Membrane dynamics and dispersion relation.—

We consider an unperturbed lipid membrane tube of radius r_0 , aligned along the z -axis. The base flow of lipids is captured by the velocity field $\mathbf{v}_{(0)} = V_0 \mathbf{e}_z$ for constant speed V_0 , and a force balance in the normal direction reveals the base surface tension is given by $\lambda_0 = p r_0 + k_b / (4r_0^2)$. Here, k_b is the bending modulus and p is the jump in the normal traction across the membrane surface, which is treated as a constant since dynamics of the surrounding fluid are not considered.

We now linearize the general membrane equations about the chosen base state, as detailed in the Supplemental Material (SM) [28, Sec. I.4]. All quantities are non-dimensionalized with r_0 , k_b , and the membrane viscosity ζ [29]—for which $\zeta r_0^2 / k_b$ is the fundamental time scale, k_b / r_0^2 is the fundamental tension scale, and inertial terms are found to be negligible in biological systems of interest [30]. Note lipid membrane tubes under tension, for which $\lambda_0 \geq 0$, are stable to all non-axisymmetric perturbations (see Ref. [20] and Sec. II.3 of the SM [28]). Consequently, only axisymmetric perturbations are considered here. In this case, the perturbed equations of motion can be combined into a single equation governing the perturbed tube radius \tilde{r} , given by [28, Sec. I.4(c)]

$$\tilde{r}_{,t} + SL \tilde{r}_{,z} = \left(\frac{\Gamma - 3/4}{4} \right) \tilde{r} + \left(\frac{\Gamma - 1/4}{4} \right) \tilde{r}_{,zz} - \frac{1}{8} \tilde{r}_{,zzzz}. \quad (1)$$

In the absence of bulk dynamics, membrane dynamics are governed by two dimensionless numbers: the Föppl–von Kármán number Γ and the Scriven–Love number SL ,

defined respectively as

$$\Gamma = \frac{\lambda_0 r_0^2}{k_b} \quad \text{and} \quad SL = \frac{\zeta V_0 r_0}{k_b}. \quad (2)$$

The Föppl–von Kármán number compares tension to bending forces [30, 31], and the recently introduced Scriven–Love number [30] compares out-of-plane viscous forces to bending forces.

At this point, we decompose the perturbed radius \tilde{r} into normal modes of the form $\sim \exp[i(qz - \omega t)]$, where q is a dimensionless wavenumber and ω is a dimensionless frequency. Substituting this decomposition into Eq. (1) leads to the dispersion relation

$$\omega = SLq + \frac{i}{4} \left[\Gamma(1 - q^2) + \frac{1}{4}(-3 + q^2 - 2q^4) \right]. \quad (3)$$

Temporal stability analysis.—Our first task is to determine how global sinusoidal perturbations to the membrane evolve in time. We assess the tube’s temporal stability with normal modes of real wavenumber, $q \in \mathbb{R}$, and complex frequency, $\omega = \omega^{(r)} + i\omega^{(i)} \in \mathbb{C}$, for which $\omega^{(r)} = SLq$ and $\omega^{(i)} = \frac{1}{4}[\Gamma(1 - q^2) + \frac{1}{4}(-3 + q^2 - 2q^4)]$. Given our normal mode decomposition, the tube is unstable when there exists a q for which $\omega^{(i)} > 0$ —a criterion which only depends on Γ . As shown in the SM [28, Sec. II.3], and corroborated by previous studies [13, 15–20], we find membrane tubes are unstable to a finite range of long wavelength perturbations when $\Gamma > \Gamma_c := 3/4$, as evident from the growth rate being $\omega^{(i)} = \frac{1}{4}(\Gamma - \Gamma_c)$ in the limit of $q \rightarrow 0$ [32]. Though the growth rate of membrane perturbations is determined only by the Föppl–von Kármán number, the real part of the dispersion relation (3) reveals that a nonzero base flow ($SL \neq 0$) leads to temporal oscillations in the membrane’s response, with frequency proportional to the base flow speed. Additionally, an axial base flow confers a directionality to the membrane tube, which can bias the spatial evolution of an initially local perturbation—bringing us to the concept of absolute and convective instabilities.

Absolute vs. convective instabilities.—Consider a membrane perturbation that is initially localized in space, as is the case when a tube is subjected to laser ablation [11] or when drugs are locally administered to an axon [14]. For any unstable tube with $\Gamma > \Gamma_c$, there is a competition between the local perturbation being (i) amplified, as characterized by Γ , and (ii) convected away from its location, captured by SL . Figure 1(a) shows how unstable systems are classified as being either *absolutely unstable* (AU) when amplification dominates convection, or *convectively unstable* (CU) when the instability is convected faster than it grows. The qualitative difference between AU and CU systems is highlighted in Fig. 1(b), in which we inquire for the long-time response as seen by a stationary observer—for example, one stationed at the vertical dashed line. In the AU case (Fig. 1(b), left column), the base flow is sufficiently small and the initial

perturbation grows to invade the entire domain. Consequently, our observer sees a deformed configuration at long times. In the CU case (Fig. 1(b), right column), on the other hand, the base flow is large enough to carry the perturbation downstream. As a result, any stationary observer may see a transient growth of the instability, yet at long times will see an unperturbed system—despite the disturbance continuing to grow as it is swept downstream. In what follows, we describe how to determine when the system transitions from being AU to CU, known as the *absolute-to-convective transition*.

To determine the boundary between domains of AU and CU membrane tubes, we carry out a spatiotemporal stability analysis following studies of instabilities in open flow systems [24, 25, 33], as detailed in the SM [28, Sec. III]. To this end, we consider normal modes with complex wavenumbers and frequencies: $q = q^{(r)} + iq^{(i)} \in \mathbb{C}$ and $\omega = \omega^{(r)} + i\omega^{(i)} \in \mathbb{C}$, as justified in Ref. [34]. By definition, the long-time membrane response seen by a stationary observer is dominated by zero group velocity perturbations—namely, those with $(d\omega/dq)|_{q_0} = 0$ and $\omega_0 = \omega(q_0)$. Here, we introduce the so-called absolute frequency $\omega_0 = \omega_0^{(r)} + i\omega_0^{(i)}$ and absolute wavenumber $q_0 = q_0^{(r)} + iq_0^{(i)}$, where (q_0, ω_0) corresponds to a saddle point of the system. If $\omega_0^{(i)} > 0$, a stationary observer sees the initial perturbation grow at long times and the system is AU, as in the left column of Fig. 1(b). On the other hand, if $\omega_0^{(i)} < 0$, a stationary observer sees the initial perturbation decay at long times and the system is CU, as in the right column of Fig. 1(b). Consequently, $\omega_0^{(i)} = 0$ at the boundary between AU and CU cylindrical membranes.

The real and imaginary parts of the two saddle point criteria, as well as the condition $\omega_0^{(i)} = 0$, are five equations relating six quantities: $\omega_0^{(r)}$, $\omega_0^{(i)}$, $q_0^{(r)}$, $q_0^{(i)}$, SL , and Γ . As detailed in Sec. III.1 of the SM [28], for any choice $\Gamma > \Gamma_c$, we solve this system of equations for $SL_{ac}(\Gamma)$: the value of the Scriven–Love number corresponding to the absolute-to-convective transition. As it turns out, however, $\omega_0^{(i)} = 0$ is a necessary but not sufficient requirement for such a transition [24, 35, 36]. Consequently, solving the aforementioned system of equations leads to both physical and spurious values of SL_{ac} . We select only physically relevant values by applying the so-called pinching point criterion [25], as detailed in the SM [28, Sec. III.2]. Our calculation of the physical values of $SL_{ac}(\Gamma)$ is shown as the boundary between AU and CU domains in Fig. 1(a). While the full analytical expression of $SL_{ac}(\Gamma)$ is lengthy and provided in Table 1 of the SM [28], we note two limiting cases: $SL_{ac} \approx \Gamma/2$ when $\Gamma \rightarrow \infty$ and $SL_{ac} \approx \frac{\sqrt{2}}{4}(\Gamma - \Gamma_c)^{1/2}$ when $\Gamma \rightarrow \Gamma_c^+$. In calculating $SL_{ac}(\Gamma)$, we also determine the absolute wavenumber $q_0(\Gamma)$ and frequency $\omega_0(\Gamma)$, which dominate the long-time dynamics as seen by a stationary observer. While SL_{ac}

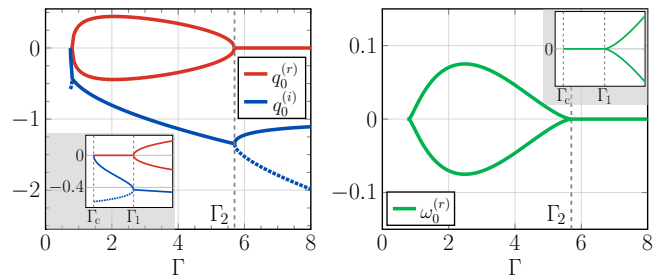


FIG. 2. Real and imaginary parts of the absolute wavenumber q_0 (left) and real part of the absolute frequency $\omega_0^{(r)}$ (right), with $\omega_0^{(i)} = 0$. The solid (resp. dashed) lines correspond to the relevant (resp. spurious) saddle points in searching for the AU/CU boundary. As the Föppl–von Kármán number increases, the bifurcation at Γ_1 signals a transition from steady to oscillatory spatiotemporal dynamics, and vice versa at Γ_2 .

is a smoothly varying function of Γ , the saddle point (q_0, ω_0) undergoes two bifurcations as Γ is varied: one at $\Gamma_1 := \frac{13}{4} - \sqrt{6} \approx 0.8$ and another at $\Gamma_2 := \frac{13}{4} + \sqrt{6} \approx 5.7$, as shown in Fig. 2 and derived in the SM [28, Sec. III.1]. We discuss how the saddle point bifurcations affect the long-time response of a perturbed lipid membrane tube in the following section on front propagation.

Front propagation.—When a membrane tube is locally perturbed, both linear simulations (Fig. 5 in the SM [28]) and nonlinear simulations [Fig. 1(b)] show the perturbed region invades the unstable, unperturbed region via a leading (+) and a trailing (−) front. We now calculate the leading and trailing front velocities V_f^\pm predicted by the linear theory. To this end, we employ the MSC [26, 27], which states that an observer traveling at the front speed would at long times see a system in its marginal state, i.e. one in which the growth rate is zero. If this observer travels at the dimensionless speed $SL_f^\pm := \zeta V_f^\pm r_0/k_b$, then they see normal modes of the form $\sim \exp[i(qz_f^\pm - \omega_f^\pm t)]$. Here, $z_f^\pm = z - SL_f^\pm t$ and $\omega_f^\pm = \omega - SL_f^\pm q$ are the Doppler-shifted axial position and frequency of the observer, respectively. At long times, the observer sees membrane dynamics dominated by modes of zero group velocity, for which $(d\omega_f^\pm/dq)|_{q_f^\pm} = 0$; here q_f^\pm are the wavenumbers associated with the leading and trailing fronts. Additionally, $\omega_f^{\pm(i)}(q_f^\pm) = 0$ in the marginal state. The aforementioned conditions in the moving frame are nearly identical to those of the AU/CU transition, and yield (see SM [28, Sec. III.5])

$$SL_f^\pm = SL \pm SL_{ac}, \quad q_f^\pm = q_0, \quad \omega_f^\pm = \omega_0 - SL_f^\pm q_f. \quad (4)$$

We now proceed to compare the linear predictions to nonlinear simulations of an axisymmetric membrane tube subject to a local perturbation. Our computations are based on the numerical method of Ref. [37], with additional details provided in the SM [28, Sec. IV.2]. Figure 1(b) shows the dynamics of an AU system ($SL = 0.25 SL_{ac}$, left) and a CU system ($SL = 2 SL_{ac}$,

right) at $\Gamma = 6$. In both cases, the leading and trailing front speeds are calculated numerically and compared to the linear prediction (4)₁, as shown in Fig. 3. It is well-known that a front can be either ‘pulled’ at the leading edge or ‘pushed’ by the growing nonlinearities behind the front, however one cannot in general anticipate which type of front will emerge from a local perturbation to invade a given nonlinear system [27, 38]. Our numerical simulations reveal the trailing edge is a pulled front, in which the front speed agrees with the MSC, while the leading edge is a pushed front traveling faster than the MSC predicts (Fig. 3). In the latter case, however, the front speed agrees with the linear theory at early times when perturbations are small (see insets in Fig. 3).

Equation (4) confirms the connection [39, 40] between the MSC and the AU/CU transition: the saddle point bifurcations shown in Fig. 2 also represent transitions in the spatiotemporal dynamics of the propagating fronts. In particular, when $\Gamma \in [\Gamma_c, \Gamma_1] \cup [\Gamma_2, \infty)$, $q_f^{(r)} = 0$ and $\omega_f^{(r)} = 0$, such that there are no oscillations in the leading edge of the front. Consequently, the front evolves as a steadily traveling envelope, as confirmed by nonlinear simulations [see Fig. 4(a),(c)]. In contrast, when $\Gamma \in (\Gamma_1, \Gamma_2)$, $q_f^{(r)} \neq 0$ and $\omega_f^{(r)} \neq 0$ —for which the front has an oscillatory structure in both time and space. As a result, a pattern is selected in the wake of the front, and a pearled morphology connects the thin and unperturbed cylindrical regions [Fig. 4(b)]. We thus find the value of the Föppl–von Kármán number governs whether or not a pattern is selected as the front propagates, which could explain why axons subjected to local laser ablation beaded in some experiments, while others atrophied and only formed long, thin tubes [14].

Weakly nonlinear analysis.—To better understand how nonlinearities affect front dynamics, we develop a weakly nonlinear model of the membrane shape evolution. In particular, for a tube with dimensionless radius $r(z, t) = 1 + \tilde{r}(z, t)$, we assume (i) $\partial_z^j \tilde{r} \cdot \partial_z^k \tilde{r}$ is negligible when $j \geq 1$ and $k \geq 1$, (ii) $\tilde{r}_{,t} \cdot \partial_z^j \tilde{r}$ is negligible when $j \geq 1$, and (iii) $\tilde{r}^j \cdot \partial_z^k \tilde{r} \ll \tilde{r}^j$ when $k \geq 1$. With these assumptions, the evolution equation for the tube radius is found to be (see SM [28, Sec. IV.1])

$$r_{,T} + \bar{S}L r_{,z} = r_{,zz} - \frac{1}{2} \frac{(\Gamma - \Gamma_c)}{(\Gamma - 1/4)^2} r_{,zzzz} + f(r), \quad (5)$$

where the nonlinear forcing term $f(r)$ is given by

$$f(r) = (r - 1) + \frac{\Gamma - 1/4}{\Gamma - \Gamma_c} (r - 1)^2 + \frac{1/4}{\Gamma - \Gamma_c} \frac{(r - 1)^2}{r} \quad (6)$$

and hereafter we refer to the coefficient of the 4th-order term as $\gamma(\Gamma) := \frac{1}{2}(\Gamma - \Gamma_c)/(\Gamma - 1/4)^2$. Equation (5) is written in terms of the rescaled variables $T = t[(\Gamma - \Gamma_c)/4]$, $Z = z[(\Gamma - \Gamma_c)/(\Gamma - 1/4)]^{1/2}$, and $\bar{S}L = 4SL/[(\Gamma - \Gamma_c)(\Gamma - 1/4)]^{1/2}$ to highlight its structure [41]. Indeed, it is clear that the evolution equation

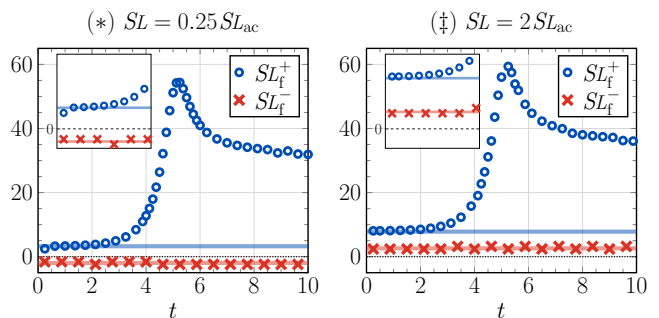


FIG. 3. Plot of leading (blue) and trailing (red) front velocities over time in the simulations shown in Fig. 1, where $\Gamma = 6$ and $SL/SL_{ac} = 0.25$ and 2 . Symbols correspond to simulations and lines are predictions from the MSC [see Eq. (4)₁]. Insets show front speeds at early times, confirming the trailing front moves to the left for $SL < SL_{ac}$ and to the right for $SL > SL_{ac}$; the leading front moves to the right in all cases.

belongs to the family of extended Fisher–Kolmogorov (EFK) equations—well-studied in the front propagation literature and known to possess several universal properties [27, 42, 43]. For example, as $\Gamma \rightarrow \Gamma_c^+$ the AU/CU transition speed of the EFK equation is given by $\bar{S}L_{ac} = 2$ [27] or equivalently $SL_{ac} \approx \frac{\sqrt{2}}{4}(\Gamma - \Gamma_c)^{1/2}$, in agreement with our earlier calculations. Moreover, the EFK equation is known to undergo steady-to-oscillatory bifurcations in the front dynamics at the universal value of $\gamma = 1/12$ [42, 43]. We confirm that $\gamma(\Gamma_1) = \gamma(\Gamma_2) = 1/12$, thus justifying the transitions in the front dynamics observed in Fig. 4. The particular values of Γ_1 and Γ_2 , for which $\gamma = 1/12$, can be understood as Lifshitz points where the q^2 term in the dispersion relation vanishes at the saddle point [44], and for which higher order gradients are required for an appropriate description of the system (see SM [28, Sec. III.6] and Refs. [43, 45]).

To understand how an oscillatory pattern emerges when $\Gamma \in (\Gamma_1, \Gamma_2)$, we recognize that γ characterizes front dynamics in the EFK equation: fronts are monotonic for $\gamma < 1/12$ and oscillatory for $\gamma > 1/12$ [42, 43]. Accordingly, the 4th-order bending term in Eq. (5) favors oscillations at the leading edge of the front. In the limit of a tube with vanishing bending modulus ($k_b \rightarrow 0$, $\Gamma \rightarrow \infty$), we find $\gamma \rightarrow 0$ —implying a monotonic front will dominate the long-time dynamics. Now imagine starting at $\Gamma \rightarrow \infty$ and steadily increasing k_b , such that Γ decreases. In doing so, Γ_2 marks where bending forces are first large enough to favor an oscillating front. As the bending modulus is further increased and $\Gamma \rightarrow \Gamma_c^+$, however, the wavelength of every unstable mode diverges (see Eq. (3), SM [28, Sec. III.3(b)]); the bending cost of such modes commensurately decreases. Thus, Γ_1 indicates where the 4th-order bending term becomes negligible once again, and we find the competition between bending forces and long-wavelength oscillations is captured by γ .

Finally, we compare predictions from the EFK model (5) with direct simulations of the full nonlinear mem-

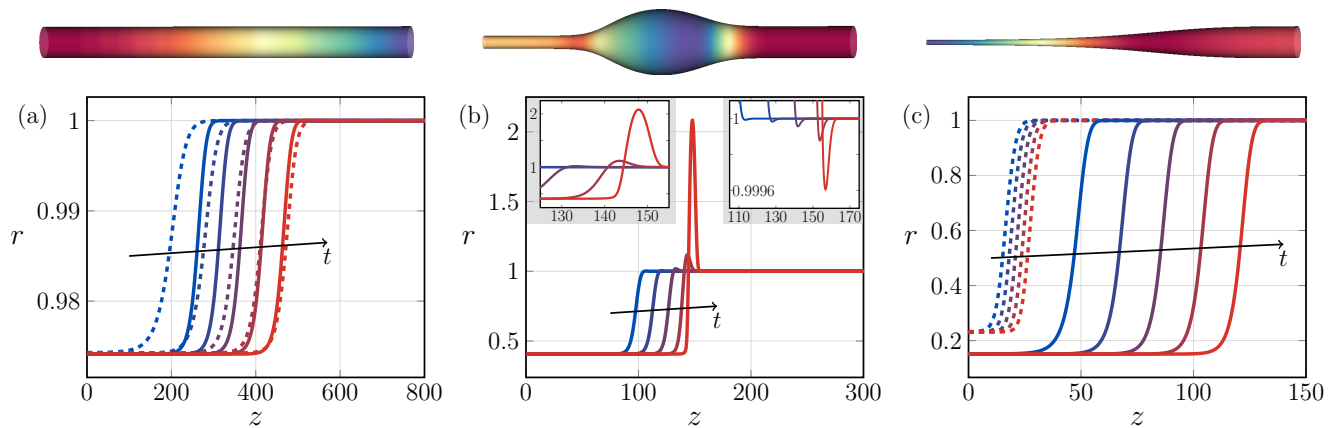


FIG. 4. Plots of the propagating fronts over time, with no base flow ($SL = 0$) and (a) $\Gamma = 0.77 \in [\Gamma_c, \Gamma_1]$, (b) $\Gamma = 2 \in (\Gamma_1, \Gamma_2)$, and (c) $\Gamma = 6 \in [\Gamma_2, \infty)$. Solid lines are results from nonlinear simulations and dotted lines are numerical predictions of the weakly nonlinear EFK equation (5). Snapshots are separated by (a) 1000τ , (b) 10τ , and (c) τ , with a portion of the three-dimensional tube at the final snapshot shown above each subplot to highlight how the atrophied region connects with the unperturbed tube. When $\Gamma \in (\Gamma_1, \Gamma_2)$ as in (b), the front leaves pearls in its wake (left inset) and oscillates at the leading edge (right inset), in agreement with the linear theory (see also Fig. 2). The EFK equation (5) best predicts the front speed and shape when $\Gamma \rightarrow \Gamma_c^+$ (a) and cannot predict shapes when $\Gamma \in (\Gamma_1, \Gamma_2)$ due to the presence of outward bulges (b).

brane equations in Fig. 4, from which we make several observations. First, both sets of dynamics result in a thin, atrophied tube behind the front. We calculate the atrophied, ‘homogeneous radius’ r_h by recognizing it varies in neither time nor space, such that our EFK equation requires $f(r_h) = 0$ —for which the only stable, physically meaningful solution is given by $r_h = 1 + (3 - 8\Gamma + \sqrt{16\Gamma - 3})/(8\Gamma - 2)$ [28, Sec. IV.1]. Thus, for all $\Gamma > \Gamma_c$, the evolution equation predicts $0 < r_h < 1$. Moreover, $r_h \rightarrow 0$ in the limit $\Gamma \rightarrow \infty$, i.e. for a fluid film with no bending modulus: a result consistent with our previous findings [46]. We also find that for $\Gamma \notin (\Gamma_1, \Gamma_2)$, the evolution equation serves as a good predictor of the front speed and final radius as $\Gamma \rightarrow \Gamma_c^+$ [Fig. 4(a)], while it only predicts r_h at large Γ [Fig. 4(c)]. On the other hand, when $\Gamma \in (\Gamma_1, \Gamma_2)$, the front oscillates at the leading edge and the quadratic forcing terms in $f(r)$ amplify outward perturbations ($r > 1$), such that the EFK model predicts an unphysical, diverging radius at finite times (see SM [28, Sec. IV.2(b)]). Despite the quantitative shortcomings of the evolution equation (5), it still provides (i) a connection to previous studies of nonlinear dynamics and pattern formation, and (ii) a qualitative understanding of front propagation. Importantly, as the evolution equation (5) gives rise to pulled fronts and agrees with nonlinear simulations when $\Gamma \rightarrow \Gamma_c^+$, we expect the front velocity of an initially static tube to scale as $SL_f \sim (\Gamma - \Gamma_c)^{1/2}$ near the instability threshold (4)₁. Such a prediction could elucidate the previously unexplained, experimentally measured front velocities near Γ_c [12, Fig. 11]. That is, while the front speed is linear with the tension over most of the unstable range, it deviates from linearity and follows $\sim (\Gamma - \Gamma_c)^{1/2}$ near the instability threshold (see SM [28, Sec. III.5]).

Conclusions.—In this Letter, we analyzed the spa-

tiotemporal stability of lipid membrane tubes, with and without a base flow. Our findings are summarized in the stability diagram in Fig. 1(a), with tubes being either stable, AU, or CU depending on the values of Γ and SL . Moreover, recalling the connection between the AU/CU transition and the well-known MSC, we showed that unstable membrane tubes possess critical Lifshitz points at which propagating fronts bifurcate from a steady to an oscillating behavior, and vice versa (Fig. 4). In the SM [28, Sec. IV], we also explore the nonlinear evolution of various types of initial perturbations (local constrictions, local expansions, and global sinusoids) by means of direct numerical simulations and analytical techniques. Our work was inspired by experimental observations of both pearled and atrophied morphologies resulting from local membrane perturbations [5, 14]. Interestingly, a previous analysis of front propagation in membrane tubes—which neglected the intramembrane viscosity yet included the bulk viscosity—always predicted a pearled configuration in unstable tubes [13]. In contrast, the present study considers only the intramembrane viscosity and finds that different patterns can be selected depending on the resting tension. Thus, a natural extension of this work is to perform a spatiotemporal stability analysis which includes both intramembrane and bulk viscosities. Advanced numerical methods, such as those presented in Ref. [46], are required to fully describe such a system.

Acknowledgements.—We thank Mr. Yannick Omar for helpful discussions regarding the axisymmetric membrane simulations, and Mr. Dimitrios Fragedakis for insightful questions. J.T. acknowledges the support of U.T. Southwestern and U.C. Berkeley. A.S. acknowledges the support of the Computational Science Graduate Fellowship from the U.S. Dept. of Energy, as well as U.C. Berkeley. K.K.M. is supported by U.C. Berkeley.

-
- * jtchoufa@berkeley.edu
 ‡ amaresah.sahu@berkeley.edu
 † kranthi@berkeley.edu
- [1] M. Terasaki, L. B. Chen, and K. Fujiwara, *J. Cell Biol.* **103**, 1557 (1986).
- [2] J. Nixon-Abell, C. J. Obara, A. V. Weigel, D. Li, W. R. Legant, C. S. Xu, H. A. Pasolli, K. Harvey, H. F. Hess, E. Betzig, C. Blackstone, and J. Lippincott-Schwartz, *Science* **354** (2016).
- [3] A. Roux, G. Cappello, J. Cartaud, J. Prost, B. Goud, and P. Bassereau, *Proc. Natl. Acad. Sci. U.S.A.* **99**, 5394 (2002).
- [4] G. Koster, M. VanDuijn, B. Hofs, and M. Dogterom, *Proc. Natl. Acad. Sci. U.S.A.* **100**, 15583 (2003).
- [5] R. Bar-Ziv, T. Tlusty, and E. Moses, *Phys. Rev. Lett.* **79**, 1158 (1997).
- [6] V. Kantsler, E. Segre, and V. Steinberg, *Phys. Rev. Lett.* **101**, 048101 (2008).
- [7] J. B. Dahl, V. Narsimhan, B. Gouveia, S. Kumar, E. S. G. Shaqfeh, and S. J. Muller, *Soft Matter* **12**, 3787 (2016).
- [8] P. A. Pullarkat, P. Dommersnes, P. Fernández, J.-F. Joanny, and A. Ott, *Phys. Rev. Lett.* **96**, 048104 (2006).
- [9] M. Yanagisawa, M. Imai, and T. Taniguchi, *Phys. Rev. Lett.* **100**, 148102 (2008).
- [10] J. Sanborn, K. Oglecka, R. S. Kraut, and A. N. Parikh, *Faraday Discuss.* **161**, 167 (2013).
- [11] R. Bar-Ziv and E. Moses, *Phys. Rev. Lett.* **73**, 1392 (1994).
- [12] R. Bar-Ziv, E. Moses, and P. Nelson, *Biophys. J.* **75**, 294 (1998).
- [13] R. E. Goldstein, P. Nelson, T. Powers, and U. Seifert, *J. Phys. II* **6**, 767 (1996).
- [14] A. Datar, J. Ameeramja, A. Bhat, R. Srivastava, A. Mishra, R. Bernal, J. Prost, A. Callan-Jones, and P. A. Pullarkat, *Biophys. J.* **117**, 880 (2019).
- [15] P. Nelson, T. Powers, and U. Seifert, *Phys. Rev. Lett.* **74**, 3384 (1995).
- [16] R. Granek and Z. Olami, *J. Phys. II France* **5**, 1349 (1995).
- [17] K. L. Gurin, V. V. Lebedev, and A. R. Muratov, *J. Expl. Theor. Phys.* **83**, 321 (1996).
- [18] T. R. Powers and R. E. Goldstein, *Phys. Rev. Lett.* **78**, 2555 (1997).
- [19] G. Boedec, M. Jaeger, and M. Leonetti, *J. Fluid Mech.* **743**, 262 (2014).
- [20] V. Narsimhan, A. Spann, and E. Shaqfeh, *J. Fluid Mech.* **777**, 1 (2015).
- [21] J. Dai and M. P. Sheetz, *Biophys. J.* **68**, 988 (1995).
- [22] J. Dai and M. P. Sheetz, *Cell* **83**, 693 (1995).
- [23] Dommersnes, P. G., Orwar, O., Brochard-Wyart, F., and Joanny, J. F., *Europhys. Lett.* **70**, 271 (2005).
- [24] A. Bers and R. J. Briggs, *Bull. Am. Phys. Soc.* **9**, 304 (1963).
- [25] P. Huerre and M. Rossi, “Hydrodynamic instabilities in open flows,” in *Hydrodynamics and Nonlinear Instabilities*, edited by C. Godrèche and P. Manneville (Cambridge University Press, 1998) pp. 81–294.
- [26] G. Dee and J. S. Langer, *Phys. Rev. Lett.* **50**, 383 (1983).
- [27] W. van Saarloos, *Phys. Rev. A* **39**, 6367 (1989).
- [28] See the Supplemental Material (SM), in which the equations of motion and dispersion relation are obtained, and the spatiotemporal stability is analyzed.
- [29] Dimensions are as follows: $[r_0]$ = length, $[k_b]$ = energy, and $[\zeta]$ = force · time/length.
- [30] A. Sahu, A. Glisman, J. Tchoufag, and K. K. Mandadapu, *Phys. Rev. E* **101**, 052401 (2020).
- [31] J. Lidmar, L. Mirny, and D. R. Nelson, *Phys. Rev. E* **68**, 051910 (2003).
- [32] The value of the dimensionless critical tension is sometimes reported as $3/2$, in cases where the bending modulus is chosen instead to be $\kappa = k_b/2$.
- [33] F. Charru, *Hydrodynamic Instabilities* (Cambridge University Press, 2011).
- [34] J. Eggers and E. Villermaux, *Rep. Prog. Phys.* **71**, 036601 (2008).
- [35] K. Kupfer, A. Bers, and A. K. Ram, *Phys. Fluids* **30**, 3075 (1987).
- [36] P. Huerre and P. A. Monkewitz, *Annu. Rev. Fluid Mech.* **22**, 473 (1990).
- [37] Y. A. D. Omar, A. Sahu, R. A. Sauer, and K. K. Mandadapu, *Biophys. J.* (2020).
- [38] W. van Saarloos, *Phys. Rep.* **386**, 29 (2003).
- [39] W. van Saarloos, “Front propagation into unstable states: Some recent developments and surprises,” in *Nonlinear Evolution of Spatio-Temporal Structures in Dissipative Continuous Systems*, edited by F. H. Busse and L. Kramer (Springer US, Boston, MA, 1990) pp. 499–508.
- [40] J.-M. Chomaz and A. Couairon, *Phys. Rev. Lett.* **84**, 1910 (2000).
- [41] The rescaled variables are only physically meaningful when $\Gamma > \Gamma_c$.
- [42] G. T. Dee and W. van Saarloos, *Phys. Rev. Lett.* **60**, 2641 (1988).
- [43] M. C. Cross and P. C. Hohenberg, *Rev. Mod. Phys.* **65**, 851 (1993).
- [44] W. Zimmermann, *Phys. Rev. Lett.* **66**, 1546 (1991).
- [45] R. M. Hornreich, M. Luban, and S. Shtrikman, *Phys. Rev. Lett.* **35**, 1678 (1975).
- [46] A. Sahu, Y. A. D. Omar, R. A. Sauer, and K. K. Mandadapu, *J. Comp. Phys.* **407**, 109253 (2020).